*metals*

MDPI

*Article*

# Investigation of Through-Thickness Residual Stress, Microstructure and Texture in Radial Forged High-Strength Alloy Steel Tubes

**Weisheng Xu and Jin Zhang ***

Institute for Advanced Materials and Technology, University of Science and Technology Beijing, Beijing 100083, China; weishengxu@foxmail.com

* Correspondence: zhangjin@ustb.edu.cn; Tel.: +86-010-82377393

**Abstract:** Gradient variations of through-thickness residual stress, microstructure and texture greatly affect the performance of cold radial forged tubes. In this work, the through-thickness distribution of residual stress was measured based on the Debye ring. The microstructure was characterized with the electron backscattering diffraction technique. The texture was measured by the X-ray diffractometer. The influence of microstructure and texture on the strength and anisotropy of forged tubes with different thickness reductions was analyzed. The results show that the residual stress varies gradually from compressive to tensile from the outer to inner surface. The microhardness of the outer surface is lower than the inner. The dislocation density and low-angle grain boundary fraction are the smallest in the one-third thickness. The dislocation density and low-angle grain boundary fraction increase gradually from the one-third thickness to the inner surface. The main texture components of the forged tube include {111}<110>, {001}<110> and {114}<110>. Texture {111}<110> deflects gradually toward {114}<110>, {112}<110> and {110}<110> from the external tube to the internal tube. The gradient variation of strength mainly resulted from the difference of the dislocation density. The difference of strength along the radial direction is reduced with a larger thickness reduction. This work has important significance for improving the performance of high-strength alloy steel tubes processed by cold radial forging.

**Keywords:** radial forging; residual stress; microstructure; texture

check for updates

**Citation:** Xu, W.; Zhang, J. Investigation of Through-Thickness Residual Stress, Microstructure and Texture in Radial Forged High-Strength Alloy Steel Tubes. *Metals* **2022**, *12*, 622. https://doi.org/10.3390/met12040622

Academic Editors: Thomas Niendorf, Zhenjia Xie, Xueda Li and Xiangliang Wan

Received: 22 March 2022
Accepted: 2 April 2022
Published: 4 April 2022

**Publisher's Note:** MDPI stays neutral with regard to jurisdictional claims in published maps and institutional affiliations.

**Copyright:** © 2022 by the authors. Licensee MDPI, Basel, Switzerland. This article is an open access article distributed under the terms and conditions of the Creative Commons Attribution (CC BY) license (https://creativecommons.org/licenses/by/4.0/).

## 1. Introduction

The performance of the barrel can be improved greatly by cold radial forging [1,2]. In the forging process, it is very common to observe the deformation gradient through the thickness [3]. The uneven deformation will result in residual stress and gradient changes of the microstructure. The through-thickness residual stress distribution has a significant impact on the product, such as strength, dimensional stability and fatigue strength [4,5]. The through-thickness texture and microstructure will also affect the performance of products. Chen et al. [6] found that texture changes along the thickness direction can lead to differences in the anisotropy. Moreover, the gradient change of texture also affects the through-thickness distribution of residual stress [7]. Gradient variations of the microstructure will cause the differences in strength, which, in turn, affect the overall performance [8]. Therefore, it is necessary to study the through-thickness variation of residual stress, microstructure and texture in cold radial forged tubes.

The simulation method was mainly adopted on the current research of radial forging [9–12]. It shows that the influence of friction is mainly on the surface residual stress. Ishkina et al. [13] found that both the residual stress and microstructure of the internal and external surface in the rotary forging steel tube were different. The research of Ghaei et al. [14] proved that the surface residual stress was reduced significantly when the mandrel was used. Xu et al. [15] worked over the effect of the radial forging process on the near surface microstructure and

texture. It indicated that the texture and anisotropy increased gradually with the increase of deformation. Arreola et al. [16] researched the impact of cold forging on the property of 32CDV13 steel. It showed that large deformation had a positive effect on the hardness yield and tensile strength. Xiao et al. [17] investigated the microstructure of the radial forged 20MnTiB steel. It was found that the ferrite grains were elongated after forging while the pearlite grains were refined. Kamikawa [18] and Barrett [19] found that the through-thickness shear texture was affected by the friction. Gao et al. [20] found that the thickness reduction had an impact on texture types and tensile strength.

Although research on the microstructure and texture of forging have been reported, these studies mainly focus on the microstructure of the surface. Research is lacking on the through-thickness residual stress, microstructure and texture. Furthermore, the influence of the through-thickness microstructure and texture on the strength and anisotropy is unclear. This work has important significance for evaluating the process optimization to improve the overall performance of forged tubes. This paper focused on the through-thickness distribution of residual stress, hardness, grain boundary, grain size, dislocation density and texture in the radial forged tube. The residual stress was measured by the XRD method based on the Debye ring. The through-thickness microstructure was characterized using the electron backscattering technique. The measurement of texture was performed on an X-ray diffractometer.

## 2. Materials and Methods

### *2.1. Materials and Cold Radial Forging*

As shown in Figure 1, the inner and outer radius of the tube before forging are represented by $R_i$ and $R_o$. The inner and outer radius of the forged tube are expressed by $r_i$ and $r_o$. The chemical composition of the tube is shown in Table 1, which is a Ni−Cr−Mo high-strength low alloy steel with a yield strength of 1000 MPa. After the forging process, the strength of the forged tube increases by 20%, which is about 1200 MPa. The dimensions of the radial forged tube are shown in Table 2. The thickness reduction $\eta$ is given by the following equation:

$$\eta = \frac{\left(R_o^2 - R_i^2\right) - \left(b^2 - a^2\right)}{R_o^2 - R_i^2} \quad (1)$$

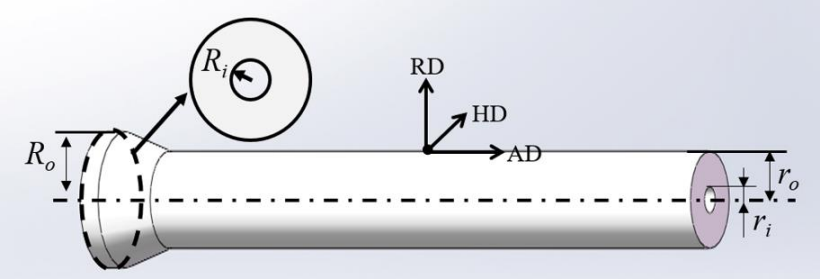



**Figure 1.** Schematic diagram of the cold radial forged tube.

**Table 1.** Chemical composition of the Ni−Cr−Mo steel (wt%).

| C | Ni | Cr | Mo | W | V | P, S |
|---|---|---|---|---|---|---|
| 0.22–0.28 | 2.60–3.20 | 1.20–2.30 | 0.45–0.75 | 0.30–0.60 | 0.15–0.35 | ≤0.01 |

**Table 2.** The dimensions of the steel tube with different thickness reductions (mm).

| $R_o$ | $R_i$ | $r_o$ | $r_i$ | $\eta$ |
|---|---|---|---|---|
| 15.10 | 5.60 | 11.00 | 2.90 | 42.7% |
| 15.10 | 5.60 | 10.45 | 2.90 | 48.7% |

### 2.2. Residual Stress Determination

The portable X-ray residual stress analyzer used in the test is a μ-X360n [21]. The target material is chromium, and the crystal plane for the measurement of residual stress is (211). E and ν are the elastic modulus and Poisson's ratio of the material, which are 225.5 GPa and 0.28 for the calculation of residual stress [22,23]. The radial residual stress of the outer surface should be 0 MPa [14]. After the axial and hoop residual stress $\sigma_z'(r)$, $\sigma_t'(r)$ at the radius r were measured, the initial axial, hoop and radial residual stress $\sigma_z(r)$, $\sigma_t(r)$, $\sigma_r(r)$ were calculated with the following formula [24,25]:

$$\sigma_z(r) = \sigma_z'(r) - 2\int_r^{r_o} \frac{r}{r^2 - {r_i}^2}\sigma_z' dr \tag{2}$$

$$\sigma_t(r) = \sigma_t'(r) - \frac{r^2 + {r_i}^2}{r^2}\int_r^{r_o} \frac{r}{r^2 - {r_i}^2}\sigma_t' dr \tag{3}$$

$$\sigma_r(r) = -\frac{r^2 - {r_i}^2}{r^2}\int_r^{r_o} \frac{r}{r^2 - {r_i}^2}\sigma_t' dr \tag{4}$$

### 2.3. Microhardness and Texture

The sections of outer surface ($r$ = 11 mm), one-third thickness ($r$ = 8.3 mm), two-thirds thickness ($r$ = 5.6 mm) and inner surface ($r$ = 2.9 mm) were selected for the measurement of the Vickers hardness (HV) and texture of the forged tube with a reduction of 42.7%, as shown in Figure 2. The hardness was measured by the hardness tester of HXD-1000. The retention time was set to 15 s, and the load was 500 g. The measurement of the texture was performed on the Bruker D8 Advance diffractometer. The different directions of the sample are shown in Figure 2. AD, HD and RD are the axial, hoop and radial direction of the forged tube.

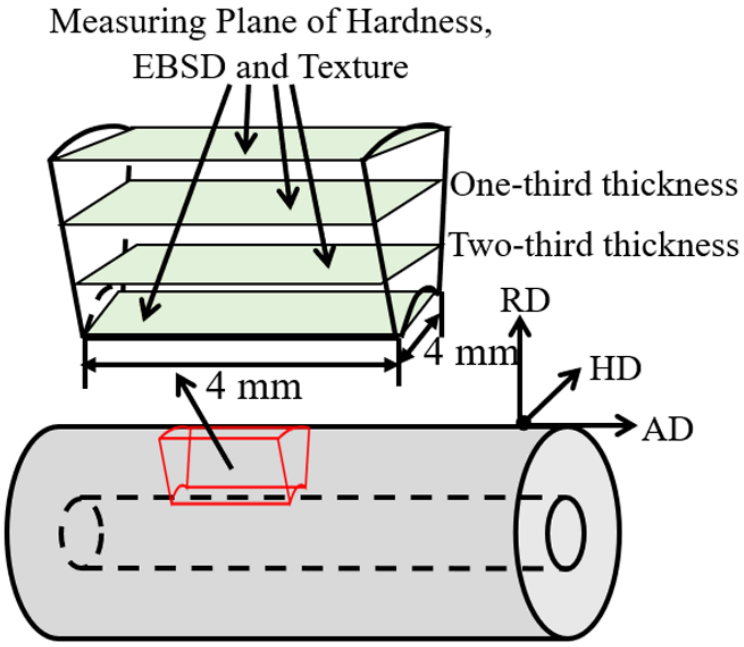



**Figure 2.** Measuring plane of hardness, EBSD and texture.

### 2.4. Microstructural Characteristics

The sections with a radius of 11, 8.3, 5.6 and 2.9 mm were selected for the observation of the microstructure of the forged tube with a reduction of 42.7%, as shown in Figure 2. The inner ($r$ = 2.9 mm) and outer ($r$ = 10.9 mm) surface were selected for the observation of the microstructure of the forged tube with a reduction of 48.7%. The microstructure of the forged tube was observed by a field emission scanning electron microscope. The

model of the electron microscope is a JSM-7100 (Oxford Instruments, Oxford, UK), which is equipped with an electron backscatter diffraction system. The solution for the electrolytic polishing was an alcohol containing 5% glycerol and 10% perchloric acid. A step size of 0.08 μm was set to scan the sample.

## 3. Results

### *3.1. Residual Stress*

The residual stress varies gradually from compressive to tensile from outside to inside, as shown in Figure 3. The hoop residual stress was smaller than the axial residual stress at the same location. The radial residual stress is less than 110 MPa. The radial residual stress of the tube satisfies the balance condition. Since the residual stress measured in this work is uniformly distributed along the circumferential direction of the tube, the tensile, radial residual stresses in opposite directions of the same radius can balance each other, so there is no need for the simultaneous existence of both tensile stress and compressive stress. The change of residual stress is large near the inner and outer surface while the stress changes slowly in the middle. The residual stress on the outer surface is compressive, and the tensile, residual stress near the inner surface is up to 728 MPa. The compressive stresses on the outer surface can prevent the propagation of a crack. The tensile stresses of the inner surface will reduce the fatigue life of the forged tube. Therefore, it is important to reduce the residual stress of the inner surface.

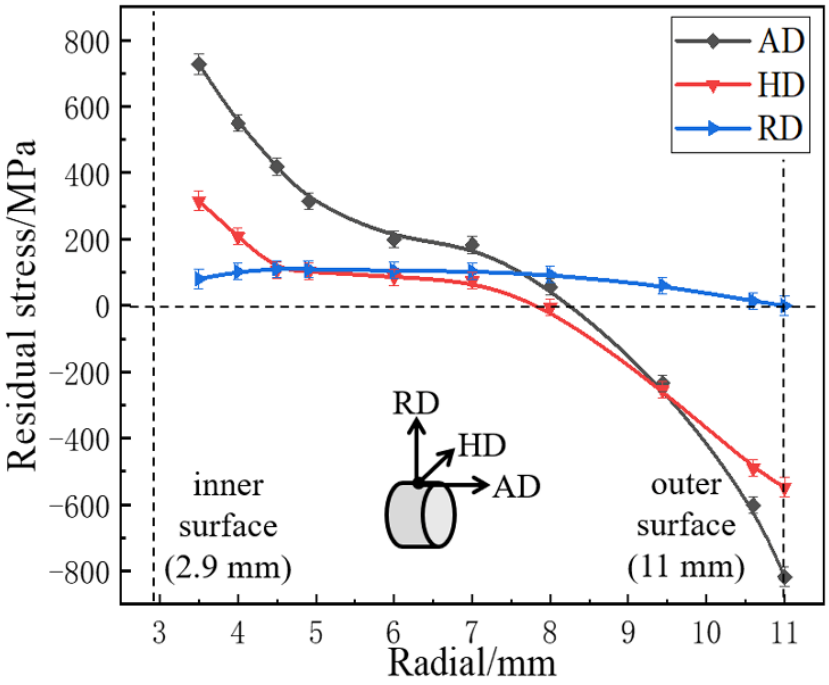



**Figure 3.** Residual stress distribution of the forged tube with a reduction of 42.7%.

### *3.2. Microhardness*

The distribution of hardness is uneven in the radial direction of the forged tube. The microhardness of the one-third thickness is lower than the inner surface, as shown in Figure 4. The increase of microhardness is caused mainly by the work hardening of metal. The uneven distribution of hardness is related to the deformation inhomogeneity through the thickness direction. The outer surface of the tube contacts directly with the hammer, and the inner surface contacts with the mandrel. The deformation of the near outer surface is small due to the friction [26]. In order to measure the distribution of microhardness along the thickness direction, a strip of 4 mm (thickness) × 4 mm (width) × 8.1 mm (height) was cut from the section of the forged tube. Since the size is small enough, the residual stress of the measured strip has been released. The influence of residual stress on the measurement

of microhardness is negligible. Therefore, there is no quantitative relationship between the microhardness and residual stress measured in this work. However, the deformation of the inner surface is greater than the outer, according to the distribution of hardness. The uneven deformation of the forged tube is the main component affecting the distribution of residual stress. When the elastic strain and stress of the outer surface is completely recovered after the external force is removed, there is still tensile, residual strain on the inner surface. Due to the restriction of the strain of the inner and outer surfaces, the outer surface is subjected to compressive residual stress, and tensile residual stress is formed on the inner surface.

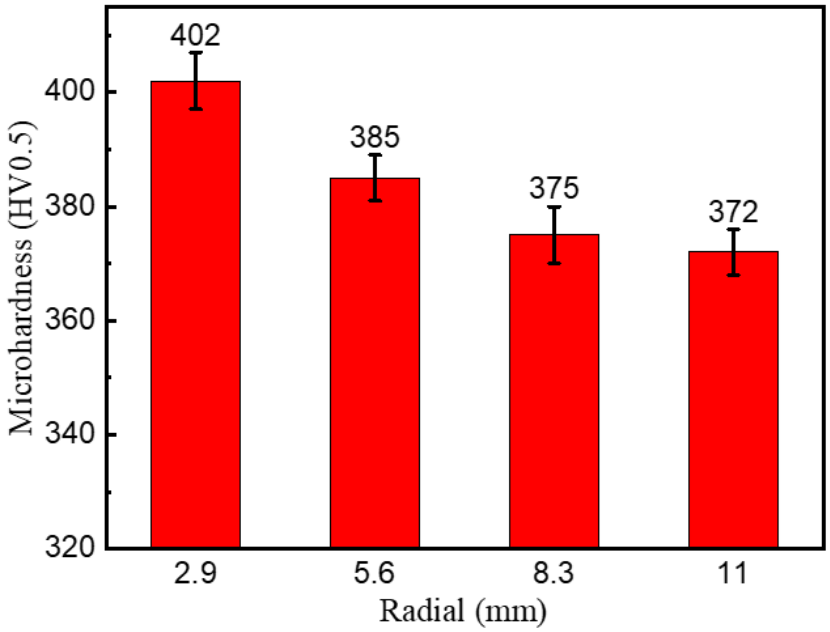



**Figure 4.** Microhardness of the forged tube with a reduction of 42.7%.

### *3.3. Microstructure Evolution*

The through-thickness deformation can be reflected by the changes of grain boundaries and grains. The grain boundaries and grains at different radial positions are shown in Figure 5a–d. The low-angle grain boundaries (LAGBs) are expressed with the white lines, which are larger than 2° and smaller than 5°. The yellow line is the medium-angle grain boundary between 5° and 15°. The black line represents the high-angle grain boundary with an orientation difference greater than 15°. The grain boundaries and grains at different radial positions are shown in Figure 5a–d. More grains are elongated along the axial direction with the increase of deformation [27].

Figure 5i–l shows the through-thickness average grain size (AGS) of the forged tube. The grain size decreases gradually from the one-third thickness to the inner surface. The relative frequency of grains smaller than 0.5 μm increased from 77% to 83%, and the average grain size decreased from 0.48 μm to 0.41 μm. The grain refinement is mainly on the inner surface. As shown in Figure 5a–d and Table 3, the distribution of the grain boundaries is uniform in the whole map. However, the low-angle grain boundaries fraction increases significantly near the inner surface. The high-angle grain boundaries are mainly between 40° and 60°, as shown in Figure 5e–h. The distribution of the medium- and low-angle grain boundaries is mainly between 2° and 10°. The low-angle grain boundary decreases gradually from the one-third thickness to the inner surface. The increase of the low-angle grain boundary will lead to an increase in the strength.

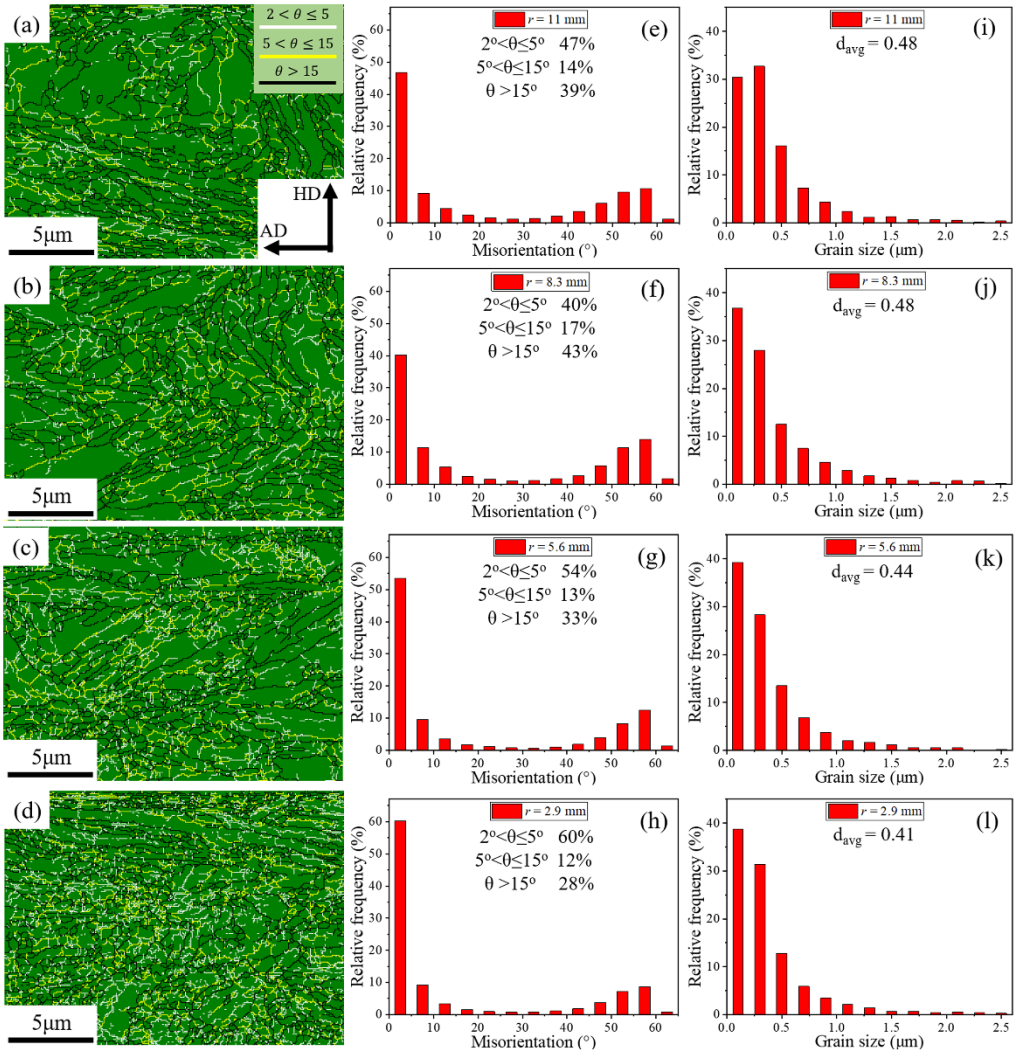



**Figure 5.** Grain boundary maps of the forged tube with a reduction of 42.7%: (**a**,**e**,**i**) $r$ = 11 mm; (**b**,**f**,**j**) $r$ = 8.3 mm; (**c**,**g**,**k**) $r$ = 5.6 mm; (**d**,**h**,**l**) $r$ = 2.9 mm.

**Table 3.** Grain boundary fraction and AGS of the forged tube with a reduction of 42.7%.

| Radial (mm) | LAGBs (%) | MAGBs (%) | HAGBs (%) | AGS (μm) |
|---|---|---|---|---|
| 11.0 | 47 | 14 | 39 | 0.48 |
| 8.3 | 40 | 17 | 43 | 0.48 |
| 5.6 | 54 | 13 | 33 | 0.44 |
| 2.9 | 60 | 12 | 28 | 0.41 |

The variation of the dislocation density is related to the deformation during forging. Figure 6 shows the local misorientation at different radial positions. The blue and red represent the low and high misorientation, as shown in Figure 6. The high local misorientation is distributed mainly near the high-angle grain boundaries. The local misorientation inside the large grains is low. The average local misorientation near the outer surface is the smallest. The local misorientation increases significantly on the inner surface. Figure 7 shows the distribution of the local misorientation. The local misorientation is distributed mainly from 0 to 2 degrees. The difference between the outer surface and one-third thickness is small. The average local misorientation increases gradually from the one-third thickness to the inner surface.

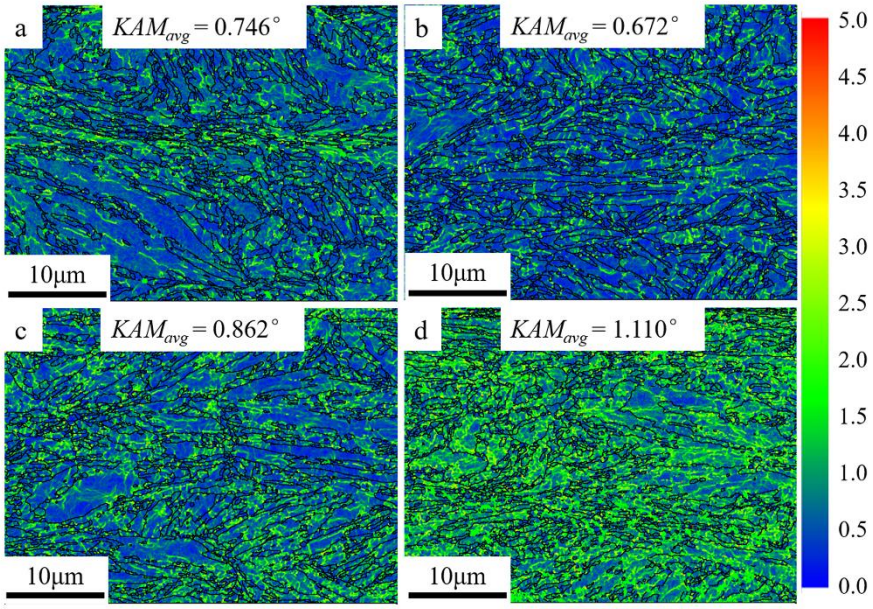



**Figure 6.** The *KAM* maps of the forged tube with a reduction of 42.7%: (**a**) $r$ = 11.0 mm; (**b**) $r$ = 8.3 mm; (**c**) $r$ = 5.6 mm; (**d**) $r$ = 2.9 mm.

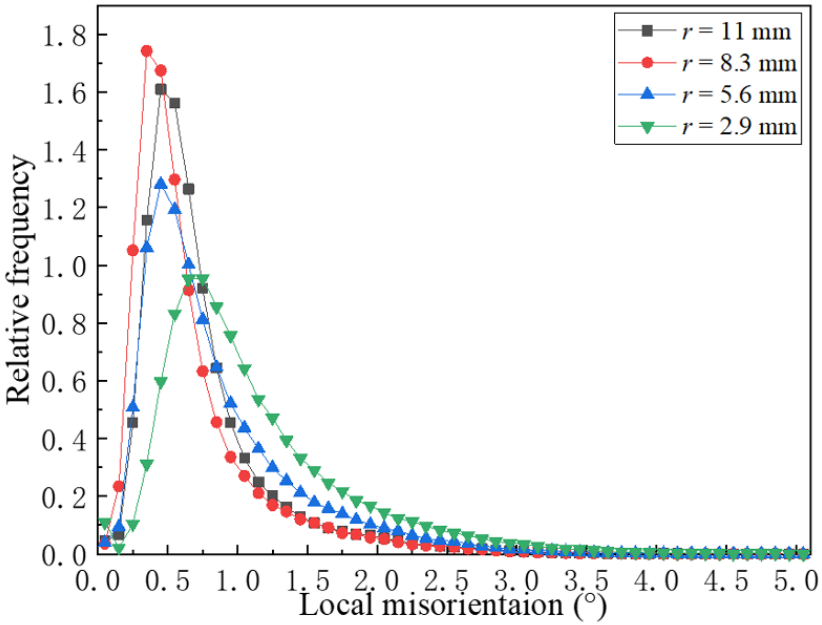



**Figure 7.** Local misorientation distribution of the forged tube with a reduction of 42.7%.

The geometric necessary dislocation (GND) density is calculated by the average local misorientation ($\theta_{KAM}$), and the formula is as follows [28]:

$$\rho_{\mathrm{GND}} \cong \frac{2\theta_{KAM}}{bd} \tag{5}$$

where the step size ($d$) is 0.08 μm in this work. The Bragg vector length ($b$) is equal to 0.248 nm for martensitic steel. The GND at different radial positions is shown in Table 4. The GND of the inner surface increases significantly. The strength will increase with the increase of the dislocation density [29,30]. The strength of the one-third thickness is the weakest as a result of the lowest dislocation density.

**Table 4.** GND of the forged tube with a reduction of 42.7%.

| Radial (mm) | 11 | 8.3 | 5.6 | 2.9 |
|---|---|---|---|---|
| GND ($10^{15}$ $m^{-2}$) | 1.31 | 1.18 | 1.52 | 1.95 |

### *3.4. Texture Evolution*

The texture of the forged tube is shown in Figure 8. The green, blue and red represent the texture of the <110>//axial direction (AD), <111>//AD and <001>//AD. The main texture component of the forged tube is texture <110>//AD (α-fiber). The intensity of the texture <110>//AD increases gradually from the one-third thickness to the inner surface. The texture <110>//AD of the one-third thickness is the weakest. Figure 9 is the 45° ODF diagram at different radial positions. The main texture of the forged tube is texture <110>//AD, texture {111}//forging surface (γ-fiber) and texture {001}//forging surface (λ-fiber). The main texture components include texture {111}<110>, {001}<110> and {114}<110>. The γ-fiber texture is more obvious on the outer surface. There are more α-fiber and λ-fiber texture on the inner surface. The thickness's uneven deformation greatly affects the distribution of texture. [31,32].

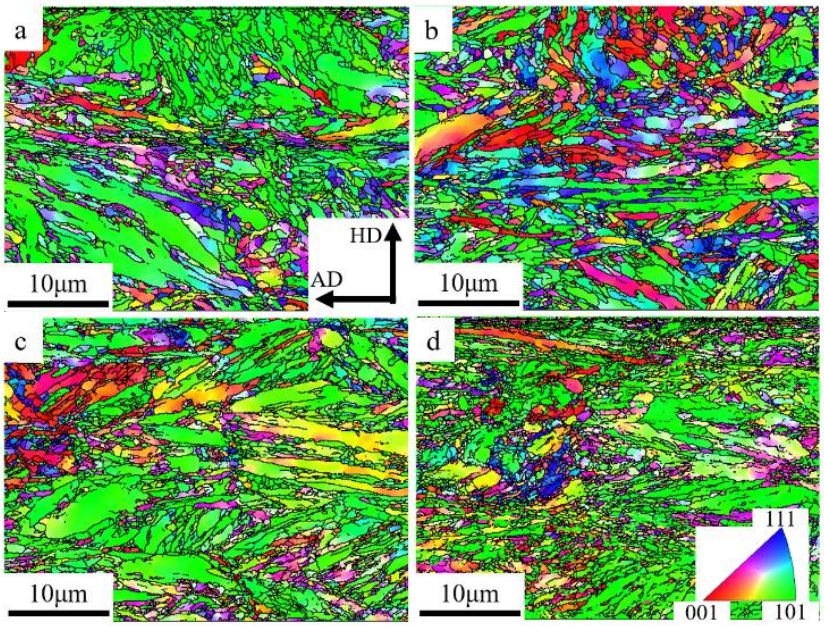



**Figure 8.** The IPFX maps of the forged tube with a reduction of 42.7%: (**a**) *r* = 11.0 mm; (**b**) *r* = 8.3 mm; (**c**) *r* = 5.6 mm; (**d**) *r* = 2.9 mm.

The orientation density distribution of different radial positions is shown in Figure 10. $\varphi_1$ is the Euler angle for the first rotation around the Z axis (RD), Φ is the Euler angle rotating around the X axis (AD) and $\varphi_2$ is the Euler angle for the second rotation around the Z axis (RD). The volume fractions of the main texture components are shown in Table 5. The proportion of various textures is different from the outside to the inside surface. The texture {001}<110> increases gradually from the outer surface to the two-third thickness. Texture {111}<110> deflects gradually toward {110}<110>, {112}<110> and {114}<110>. The shear texture [33] {001}<110> is larger in the one-third and two-third thickness. The larger the shear deformation, the more obvious the shear texture. Friction has an influence on the shear texture. The shear texture can be reduced by lubrication [19]. Shear deformation occurs at the interface of the thickness reduction zone of the inner and outer wall [20]. The one-third thickness is sheared by the deformation of the inner and outer wall, resulting in the forming of a shear texture.

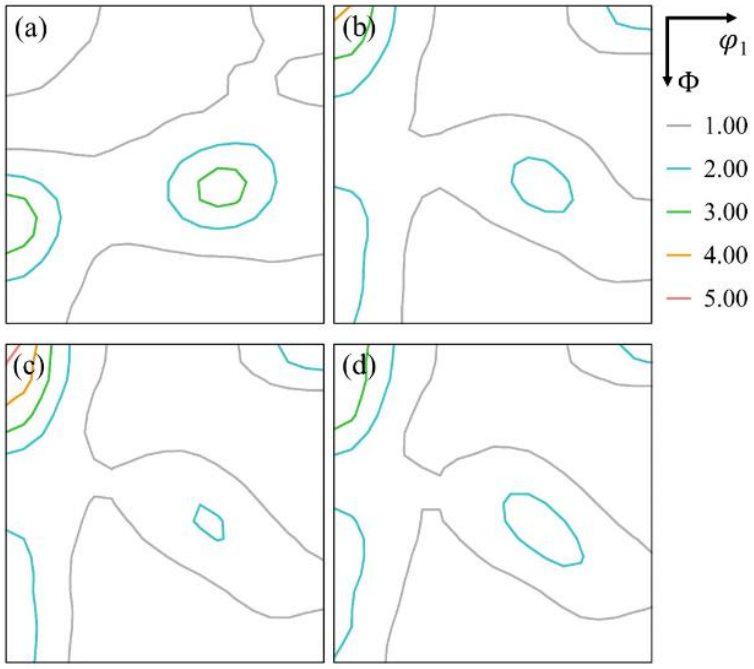



**Figure 9.** The 45° ODF diagrams of the forged tube with a reduction of 42.7%: (**a**) $r$ = 11.0 mm; (**b**) $r$ = 8.3 mm; (**c**) $r$ = 5.6 mm; (**d**) $r$ = 2.9 mm.

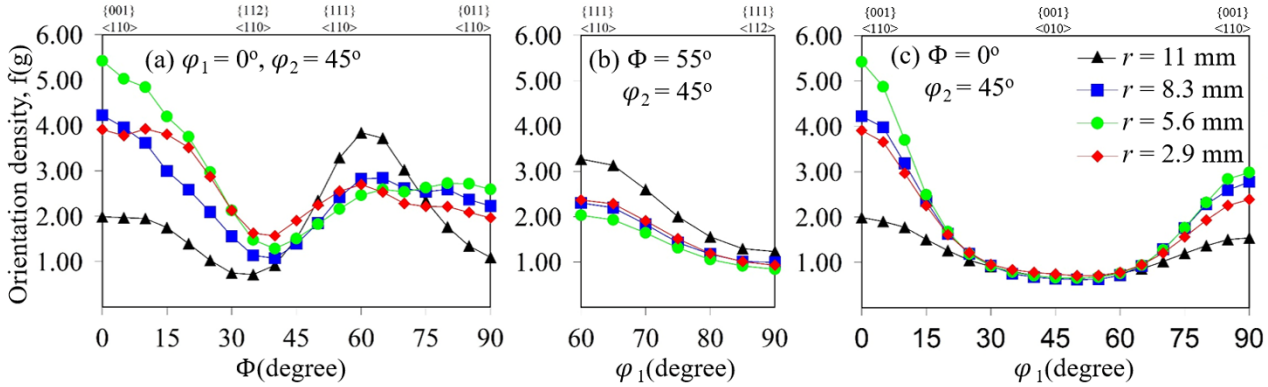



**Figure 10.** Orientation density distribution along various orientation lines in the forged tube with a reduction of 42.7%: (**a**) α-fiber orientation; (**b**) γ-fiber orientation; (**c**) λ-fiber orientation.

**Table 5.** Volume fractions of the main texture components of the forged tube with a reduction of 42.7% (%).

| Texture Component | {112} <110> | {223} <110> | {111} <110> | {110} <110> | {001} <110> | {114} <110> | {111} <011> | {001} <110> | α-fiber | γ-fiber | λ-fiber |
|---|---|---|---|---|---|---|---|---|---|---|---|
| **Euler Angle** | **(0, 30, 45)** | **(0, 45, 45)** | **(0, 57, 45)** | **(0, 90, 45)** | **(0, 0, 45)** | **(0, 20, 45)** | **(60, 55, 45)** | **(90, 0, 45)** | **-** | **-** | **-** |
| 11 mm | 3.62 | 6.48 | 10.85 | 2.66 | 3.41 | 4.92 | 10.50 | 3.40 | 14.68 | 22.15 | 11.89 |
| 8.3 mm | 5.48 | 5.77 | 8.14 | 3.93 | 5.29 | 7.77 | 7.96 | 5.28 | 16.75 | 17.41 | 14.43 |
| 5.6 mm | 6.46 | 5.91 | 7.47 | 4.28 | 5.59 | 9.00 | 7.38 | 5.57 | 16.62 | 16.30 | 14.92 |
| 2.9 mm | 6.56 | 6.96 | 8.27 | 3.55 | 4.65 | 8.30 | 8.37 | 4.64 | 15.37 | 18.13 | 13.92 |

## 4. Discussion

### *4.1. Relationship of Through-Thickness Microstructure and Residual Stresses*

The GND, LAGB fraction and local misorientation decrease from the outer surface to the one-third thickness and then increase gradually from the one-third thickness to the

inner surface. There is the smallest GND, LAGB and average local misorientation in the one-third thickness. According to the variation of the microstructure, the deformation of the inner surface is larger than the outer. Due to the uneven deformation, a strong shear texture is formed in the middle layer. There is the smallest deformation where the residual stress is close to 0 MPa. The more through-thickness deformation inhomogeneity, the greater residual stress on the outer surface. Therefore, the residual stress can be used to analyze the deformation inhomogeneity of the forged tube.

### *4.2. Effect of Through-Thickness Microstructure on Strength*

The strength of the tube increases with the increase of the dislocation density and grain refinement. The dislocation strengthening ($\Delta\sigma_\rho$) and grain boundary strengthening ($\Delta\sigma_{GB}$) can be calculated with the dislocation density ($\rho$) and average grain size ($D$) [34–36]:

$$\Delta\sigma_\rho = \alpha M \mu b \rho^{1/2} \tag{6}$$

$$\Delta\sigma_{GB} = 17.402 D^{-1/2} \tag{7}$$

where the constant $\alpha$ is equal to 0.23. For martensitic steels with body-centered cubic crystal, $M$ (Taylor factors), $\mu$ (shear modulus) and $b$ (mode of Burgers vector) are equal to 2.9, 88 GPa and 0.248 nm.

According to the Equations (6) and (7), the influence of dislocation and grain boundary strengthening on the strength are shown in Table 6. As shown in Table 6, since the grain size is greater than 100 nm, the grain boundary strengthening has little effect on the thickness gradient of strength. The gradient change of strength along the thickness is related to the dislocation strengthening. The strength of the one-third thickness ($r$ = 8.3 mm) is the weakest. The strength of the inner surface is the largest. Uneven deformation leads to different dislocation densities of the inner and outer surfaces. Different dislocation densities result in the gradient change of strength. It has a great effect on the performance of the tube whether or not the strength of the one-third thickness is improved.

**Table 6.** The dislocation and grain boundary strengthening of the forged tube with a reduction of 42.7% (MPa).

| Radial (mm) | 11 | 8.3 | 5.6 | 2.9 |
|---|---|---|---|---|
| $\Delta\sigma_\rho$ | 527 | 500 | 568 | 643 |
| $\Delta\sigma_{GB}$ | 25 | 25 | 26 | 27 |

### *4.3. Through-Thickness Texture and Anisotropy*

The larger the Taylor factor, the more deformation energy needs to be consumed for deformation. Figure 11 shows the Taylor factor distribution of different tensile directions. The red indicates a high Taylor factor, and the yellow indicates a low Taylor factor. As shown in Figure 11, the axial Taylor factor is greater than the hoop. There is little difference in the hoop Taylor factor at different radial positions. The outer surface is the most difficult to deform since there is the highest Taylor factor while the one-third thickness is the easiest to deform for the lower Taylor factor.

The anisotropy is caused mainly by the texture {111}<110>, {110}<110>, {112}<110>, {223}<110> and {114}<110>, of which the hoop Taylor factor is lower than the axial [15]. The through-thickness variation of different textures results in a difference of the average Taylor factor, which leads to the change of the anisotropy. Table 7 shows the average Taylor factor of different radial positions. As shown in Table 7, the difference between the axial and hoop Taylor factors of the outer surface is the largest. The anisotropy of the outer surface is the most obvious. The anisotropy of the near outer surface is the smallest difference between the axial and hoop Taylor factors.

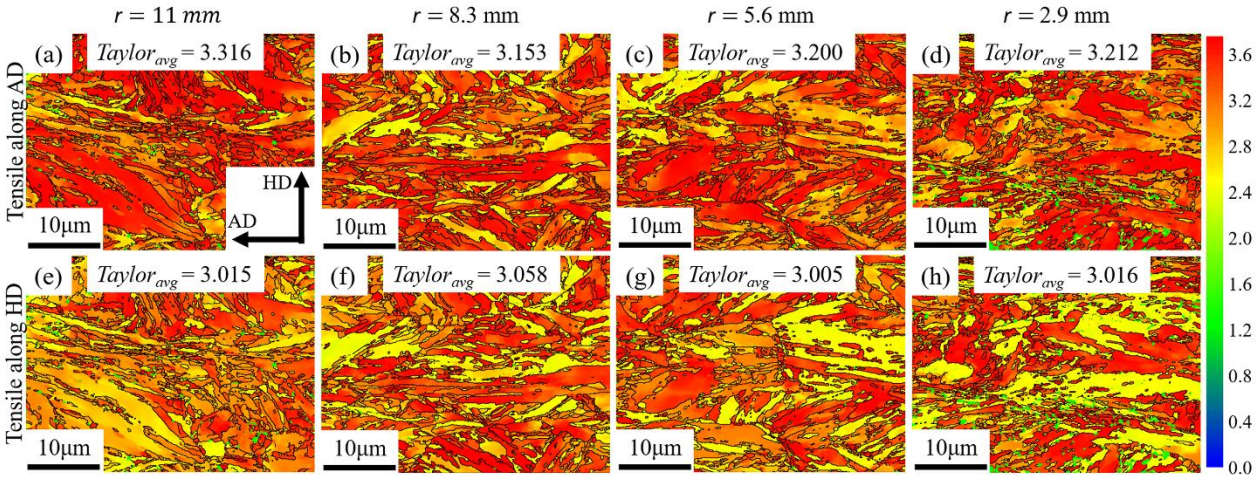



**Figure 11.** The Taylor factor distribution of the forged tube with a reduction of 42.7%: (**a**–**d**) tensile along AD; (**e**–**h**) tensile along HD.

**Table 7.** The average Taylor factor of the forged tube with a reduction of 42.7%.

| Radial (mm) | | 11 | 8.3 | 5.6 | 2.9 |
|---|---|---|---|---|---|
| Tensile direction | AD | 3.316 | 3.153 | 3.200 | 3.212 |
| | HD | 3.015 | 3.058 | 3.005 | 3.016 |

### *4.4. Influence of Thickness Reduction on Strength and Anisotropy*

The performance of the forged tube is affected mainly by the gradient change of dislocation density and texture. The uneven deformation can be improved with a larger deformation [37]. Figure 12 shows the distribution of the Taylor factor and local misorientation with a larger thickness reduction of 48.7%, as shown in Table 2.

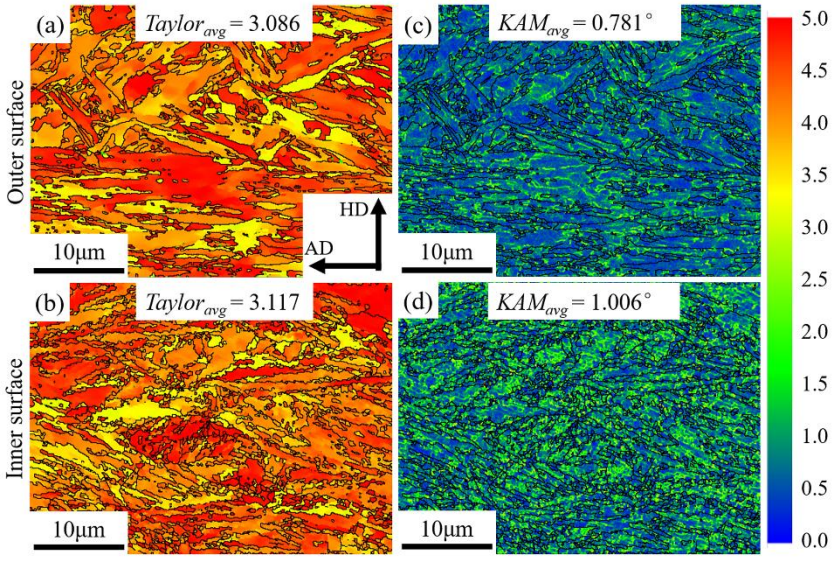



**Figure 12.** The Taylor factor distribution and *KAM* maps of the forged tube with a reduction of 48.7%: (**a**,**b**) aylor factor distribution; (**c**,**d**) *KAM* maps.

Compared with Figure 11, the difference of the axial Taylor factor between the inner and outer surfaces is reduced. The unevenness of the anisotropy along the thickness direction is reduced. Compared with Figure 6, the local misorientation of the outer surface increases, and the local misorientation of the inner surface decreases. The microhardness and dislocation strengthening are shown in Table 8. It can be seen from Table 8 that

the strength of the outer surface is enhanced with a larger thickness reduction rate. The difference of strength along the thickness direction is reduced. It is beneficial to improve the overall performance of the forged tube with a larger thickness reduction.

**Table 8.** The HV, *GND* and dislocation strengthening of the forged tube with a reduction of 48.7%.

| Position | $HV_{500}$ | GND ($10^{15}$ $m^{-2}$) | $\Delta\sigma_\rho$(MPa) |
|---|---|---|---|
| Outer surface | 376 | 1.37 | 539 |
| Inner surface | 396 | 1.77 | 612 |

## 5. Conclusions

In this paper, the through-thickness distribution of residual stress, hardness, grain boundary, grain size, dislocation density and texture in the radial forged tube was studied. The main conclusions of this work are summarized as follows:

(1) The microhardness of the outer surface is lower than the inner. There is a tensile, residual stress up to 728 MPa near the inner surface. The residual stress on the outer surface is compressive. The axial and hoop residual stress of the one-third thickness ($r$ = 8.3 mm) are close to 0 MPa.

(2) The main texture components of the forged tube include texture {111}<110>, {001}<110> and {114}<110>. From the outer to inner surface, texture {111}<110> deflects gradually toward {114}<110>, {112}<110> and {110}<110>. There is a larger shear texture {001}<110> in the middle layer than the inner and outer surface. The anisotropy of the outer surface is the most obvious.

(3) There is the smallest GND and LAGB fraction in the one-third thickness of the forged tube. The GND and LAGB increase gradually from the one-third thickness to the inner surface. The variation of the through-thickness strength mainly resulted from the difference of dislocation density. The strength inhomogeneity in the radial direction is reduced with a larger thickness reduction.

**Author Contributions:** W.X. performed the experiments; W.X. and J.Z. analyzed the data; W.X. wrote the paper. All authors have read and agreed to the published version of the manuscript.

**Funding:** This research received no external funding.

**Data Availability Statement:** Not applicable.

**Conflicts of Interest:** The authors declare no conflict of interest.

## References

1. Huang, J.; Slater, C.D.; Mandral, A.; Blackwell, P. A Dynamic Model for Simulation of Hot Radial Forging Process. *Procedia Eng.* **2017**, *207*, 478–483. [CrossRef]
2. Yang, Y.; Fan, L.; Xu, C.; Dong, X. Experimental Study of Mechanical Properties of 30SiMn2MoVA Steel Gun Barrel Processed by Cold Radial Forging. *J. Press. Vessel Technol.* **2020**, *143*, 011501. [CrossRef]
3. Kumar, G.; Lodh, A.; Singh, J.; Singh, R.; Srivastava, D.; Dey, G.; Samajdar, I. Experimental characterization and finite element modeling of through thickness deformation gradient in a cold rolled zirconium sheet. *CIRP J. Manuf. Sci. Technol.* **2017**, *19*, 176–190. [CrossRef]
4. Zhu, J.J.; Yuan, W.H. Effect of Pre-Stretching on Residual Stresses and Microstructures of Inconel 718 Superalloy. *Metals* **2021**, *11*, 614. [CrossRef]
5. Chu, Q.B.; Kong, X.F.; Tan, W. Introducing Compressive Residual Stresses into a Stainless-Steel T-Pipe Joint by an Overlay Weld. *Metals* **2021**, *11*, 1109. [CrossRef]
6. Chen, J.; Poole, W.J.; Parson, N.C. The effect of through thickness texture variation on the anisotropic mechanical response of an extruded Al-Mn-Fe-Si alloy. *Mater. Sci. Eng. A* **2018**, *730*, 24–35. [CrossRef]
7. Zdunek, J.; Maj, P.; Kulczyk, M.; Mizera, J. Texture, residual stresses and mechanical properties analysis in the commercial 1.4462 duplex stainless steel subjected to hydrostatic extrusion. *Arch. Civ. Mech. Eng.* **2019**, *19*, 525–534. [CrossRef]
8. Olivier, L.; Andrei, K.; Vladimir, L. Microstructural, Mechanical, Texture and Residual Stress Characterizations of X52 Pipeline Steel. *Metals* **2017**, *7*, 306.

9. Jang, D.; Liou, J. Study of stress development in axi-symmetric products processed by radial forging using a 3-D non-linear finite-element method. *J. Mater. Process. Technol.* **1998**, *74*, 74–82. [CrossRef]
10. Mungi, M.; Rasane, S.; Dixit, P. Residual stresses in cold axisymmetric forging. *J. Mater. Process. Technol.* **2003**, *142*, 256–266. [CrossRef]
11. Ameli, A.; Movahhedy, M.R. A parametric study on residual stresses and forging load in cold radial forging process. *Int. J. Adv. Manuf. Technol.* **2006**, *33*, 7–17. [CrossRef]
12. Wu, Y.; Dong, X. An upper bound model with continuous velocity field for strain inhomogeneity analysis in radial forging process. *Int. J. Mech. Sci.* **2016**, *115–116*, 385–391. [CrossRef]
13. Ishkina, S.; Charni, D.; Herrmann, M.; Liu, Y.; Epp, J.; Schenck, C.; Kuhfuss, B.; Zoch, H.-W. Influence of Process Fluctuations on Residual Stress Evolution in Rotary Swaging of Steel Tubes. *Materials* **2019**, *12*, 855. [CrossRef] [PubMed]
14. Ghaei, A.; Movahhedy, M.; Taheri, A.K. Finite element modelling simulation of radial forging of tubes without mandrel. *Mater. Des.* **2008**, *29*, 867–872. [CrossRef]
15. Yang, Y.; Fan, L.; Xu, C. The microstructure, texture evolution and plasticity anisotropy of 30SiMn2MoVA high strength alloy steel tube processed by cold radial forging. *Mater. Charact.* **2020**, *169*, 110641. [CrossRef]
16. Arreola-Herrera, R.; Cruz-Ramírez, A.; Suárez-Rosales, M.; Sánchez-Álvarado, R.G. The effect of cold forming on structure and properties of 32 CDV 13 steel by radial forging process. *Mater. Res.* **2014**, *17*, 445–450. [CrossRef]
17. Xiao, Z.; Liu, H.; Liu, B.; Sun, H.; Liu, D.; Liu, G. The effect of forming parameter on multi-stage cold forging with 20MnTiB steel. *Int. J. Adv. Manuf. Technol.* **2015**, *83*, 1189–1197. [CrossRef]
18. Kamikawa, N.; Tsuji, N.; Minamino, Y. Microstructure and texture through thickness of ultralow carbon IF steel sheet severely deformed by accumulative roll-bonding. *Sci. Technol. Adv. Mater.* **2004**, *5*, 163–172. [CrossRef]
19. Barrett, C. Influence of lubrication on through thickness texture of ferritically hot rolled interstitial free steel. *Ironmak. Steelmak.* **1999**, *26*, 393–397. [CrossRef]
20. Gao, X.; Wu, H.-B.; Liu, M.; Zhang, Y.-X.; Gao, F.; Zhou, X.-D. Effect of Thickness Reduction on Microstructure and Properties of Rolled C71500 Cupronickel Alloy Tube. *J. Mater. Eng. Perform.* **2021**, *30*, 3273–3283. [CrossRef]
21. Xu, W.; Mo, J.; Zhang, J.; Lian, Y.; Ji, P. Evolution of Residual Stress and Microstructure during Annealing of 30SiMn2MoVA High-Strength Alloy Steel Tube Processed by Cold Radial Forging. *J. Mater. Eng. Perform.* **2021**, *30*, 5889–5897. [CrossRef]
22. Thibault, D.; Bocher, P.; Thomas, M.; Gharghouri, M.; Côté, M. Residual stress characterization in low transformation temperature 13%Cr–4%Ni stainless steel weld by neutron diffraction and the contour method. *Mater. Sci. Eng. A* **2010**, *527*, 6205–6210. [CrossRef]
23. Woo, W.; Em, V.T.; Seong, B.S.; Mikula, P.; An, G.B. Residual stress determination in a thick ferritic steel weld plate using neutron diffraction. *J. Mater. Sci.* **2012**, *47*, 5617–5623. [CrossRef]
24. Kamal, S.M.; Borsaikia, A.C.; Dixit, U.S. Experimental assessment of residual stresses induced by the thermal autofrettage of thick-walled cylinders. *J. Strain Anal. Eng. Des.* **2015**, *51*, 144–160. [CrossRef]
25. Skvortsov, V.; Boznak, A.; Kim, A.; Arlyapov, A.Y.; Dmitriev, A. Reduction of the residual stresses in cold expanded thick-walled cylinders by plastic compression. *Def. Technol.* **2016**, *12*, 473–479. [CrossRef]
26. Goloujeh, M.R.; Soltanpour, M. Simple shear forging as a method for severe plastic deformation. *Int. J. Light. Mater. Manuf.* **2020**, *4*, 165–178. [CrossRef]
27. Zhang, K.; Marthinsen, K.; Holmedal, B.; Aukrust, T.; Segatori, A. Through thickness variations of deformation texture in round profile extrusions of 6063-type aluminium alloy: Experiments, FEM and crystal plasticity modelling. *Mater. Sci. Eng. A* **2018**, *722*, 20–29. [CrossRef]
28. Shamsujjoha, M.; Agnew, S.R.; Fitz-Gerald, J.M.; Moore, W.R.; Newman, T.A. High Strength and Ductility of Additively Manufactured 316L Stainless Steel Explained. *Met. Mater. Trans. A* **2018**, *49*, 3011–3027. [CrossRef]
29. Hwang, J.K. Correlation of Strain Path, Texture, Twinning, and Mechanical Properties in Twinning-Induced Plasticity Steel during Wire Drawing. *Materials* **2020**, *13*, 2250. [CrossRef]
30. Das, A.; Verma, V.; Basak, C.B. Elucidating microstructure of spinodal copper alloy through annealing. *Mater. Charact.* **2016**, *120*, 152–158. [CrossRef]
31. Zhang, K.; Zhang, K.; Zhu, Y.; Wu, X.; Williams, J.; Liang, E.; Ma, J.; Zhang, R.; Lim, C.V.S.; Huang, A. Effect of Deformation Reduction on Microstructure, Texture, and Mechanical Properties of Forged Ti-6Al-4V. *J. Mater. Eng. Perform.* **2021**, *30*, 1147–1156. [CrossRef]
32. Guo, X.; Wang, L.; Wang, M.; Qin, J.; Zhang, D.; Lu, W. Effects of degree of deformation on the microstructure, mechanical properties and texture of hybrid-reinforced titanium matrix composites. *Acta Mater.* **2012**, *60*, 2656–2667. [CrossRef]
33. Grydin, O.; Anatolii, A.; Briukhanov, A.; Briukhanova, Z.; Schaper, M. Evolution of Microstructure, Properties and Texture of a Two-Phase Low-Carbon Steel at Cold Asymmetric Rolling. *Steel Res. Int.* **2017**, *88*, 1600397. [CrossRef]
34. Wang, Y.-Q.; Zhang, X.-M.; He, Z.; Zu, G.-Q.; Ji, G.-F.; Duan, J.-Y.; Misra, R. Effect of copper precipitates on mechanical and magnetic properties of Cu-bearing non-oriented electrical steel processed by twin-roll strip casting. *Mater. Sci. Eng. A* **2017**, *703*, 340–347. [CrossRef]
35. Pavel, K.; Gunnel, F.; Krister, S.; Igor, Y.; Ina, Y.; Mattias, T.; Ru, P. Microstructure, Solidification Texture, and Thermal Stability of 316 L Stainless Steel Manufactured by Laser Powder Bed Fusion. *Metals* **2018**, *8*, 643.

36. Yen, H.-W.; Chen, P.-Y.; Huang, C.-Y.; Yang, J.-R. Interphase precipitation of nanometer-sized carbides in a titanium–molybdenum-bearing low-carbon steel. *Acta Mater.* **2011**, *59*, 6264–6274. [CrossRef]
37. Wang, Y.; Zhang, Y.-X.; Lu, X.; Fang, F.; Cao, G.-M.; Li, C.-G.; Xu, Y.-B.; Misra, R.D.K.; Wang, G.-D. Effect of Hot Rolling on Texture, Precipitation, and Magnetic Properties of Strip-Cast Grain-Oriented Silicon Steel. *Steel Res. Int.* **2016**, *87*, 1601–1608. [CrossRef]